



Catalytic combustion of CVOCs over $\text{MoO}_x/\text{CeO}_2$ catalysts

Hao Zhang^a, Xiaohui Gao^a, Binwei Gong^a, Shijie Shao^a, Chensheng Tu^a, Jun Pan^b, Yangyang Wang^b, Qiguang Dai^a, Yanglong Guo^{a,*}, Xingyi Wang^{a,*}

^a Research Institute of Industrial Catalysis, School of Chemistry and molecular Engineering, East China University of Science and Technology, Shanghai 200237, PR China

^b Aviation Electromechanical System Integration of Aviation Science and Technology Key Laboratory, Nanjing 211106, PR China



ARTICLE INFO

Keywords:
1,2-chloroethane
Molybdenum
Ceria
Chlorination
Catalytic combustion

ABSTRACT

$\text{MoO}_x/\text{CeO}_2$ catalysts prepared by impregnation with $(\text{NH}_4)_6\text{H}_8\text{Mo}_7\text{O}_{28}$ aqueous solution were applied for catalytic oxidation of 1,2-dichloroethane. MoO_x exists on CeO_2 fluorite as isolated $(\text{O}=\text{)}_2\text{Mo}(\text{O-Ce})_2$, poly MoO_4 and nano-particles, of which $(\text{O}=\text{)}_2\text{Mo}(\text{O-Ce})_2$ presents high acidity and reducibility of Mo, and decreases the basicity of CeO_2 , leading to the formation of reactive intermediate during 1,2-dichloroethane adsorption. The activity of $\text{MoO}_x/\text{CeO}_2$ catalysts for 1,2-dichloroethane oxidation increases with acidity and surface oxygen from CeO_2 domain. The catalyst with 2.6 Mo atom nm^{-2} presents the highest apparent activity with T_{90} of 280 °C in feed containing 1000/2000 ppm 1,2-dichloroethane at 60,000 h^{-1} space velocity. For chlorinated aromatic oxidation, similar high stable activity is observed. The ability of $(\text{O}=\text{)}_2\text{Mo}(\text{O-Ce})_2$ for water dissociation promotes Cl removal, and thus, the chlorination is inhibited completely within experiment temperature. $\text{Mo}^{6+}-\text{O}$ of $(\text{O}=\text{)}_2\text{Mo}(\text{O-Ce})_2$ is highly stable in wet feed, leading to high resistance of $\text{MoO}_x/\text{CeO}_2$ catalysts to water.

1. Introduction

Chlorinated volatile organic compounds (CVOCs), such as chlorinated aromatics (chlorobenzene (CB), 1,2-dichlorobenzene (1,2-DCB)), chlorinated alkanes (dichloromethane (DCM) and 1,2-dichloroethane (1,2-DCE)) and alkenes (vinyl chloride (VC) and trichloroethylene (TCE)), which originate from waste incineration, chlorine bleaching and other industrial processes, are extremely hazardous contaminants, due to their potential toxicity as carcinogens and teratogens, and bioaccumulation in animals and long-term persistence in the environment. Stringent environmental regulations have been imposed on the emissions containing such compounds in many countries [1]. Generally, the catalytic combustion is thought to be one of the most promising technologies for the removal of CVOCs in the emissions, due to its high efficiency and low consumption of energy when compared to a thermal process [1,2].

Noble metal catalysts were highly active for CVOC's catalytic combustion. However, they were susceptible to the adsorption of inorganic chlorine species formed during the decomposition of CVOCs, and thus showed high selectivity for chlorination [3]. Suitable Brønsted acidity and pore structure of molecular sieve catalysts could promote the adsorption and activation of CVOCs, but the deposition of coke on

Brønsted acid led inevitably to the deactivation of these catalysts [4]. The transition metal oxides, such as Co [5], Mn [6], Cr [7], Fe [8] and V [9], were resistant to chlorine poisoning, and thus used often for CVOC's catalytic combustion. In our previous work, Ce-based catalysts showed high activity for catalytic combustion of chlorinated aromatics, due to the unique reducibility and activity for C-Cl dissociation [10]. However, Cl adsorbed strongly on the surface could be removed as Cl_2 only at high temperature through Deacon reaction ($\text{HCl} + \text{O}_2 \rightarrow \text{Cl}_2 + \text{H}_2\text{O}$) [11]. Additionally, in the oxidation of chlorinated alkanes, such as DCM and 1,2-DCE, Ru/CeO₂ catalysts presented high stable activity, due to their high activity for Deacon reaction [12]. However, a considerable volatility of Ru at high temperature could limit the industrial application of Ru for catalytic combustion of CVOCs.

Molybdenum as heterogeneous catalysts were commercially applied for catalytic oxidation, such as the preparation of formaldehyde by methanol oxidation, and the preparation of acrolein and acrylic acid by propylene selective oxidation/ammonoxidation. The use of Mo-containing catalysts has been extended interestingly to lower alkanes selective oxidation [13,14]. Moreover, Mo-containing heteropoly compounds with Keggin/Anderson structures were widely investigated due to their special redox/acidic catalytic properties [15]. It was found also that Mo doped into Ce and Fe mixed oxides promoted the activation of

* Corresponding authors.

E-mail addresses: yguo@ecust.edu.cn (Y. Guo), wangxy@ecust.edu.cn (X. Wang).

gaseous oxygen to compensate the lattice oxygen consumed in NH_3 -SCR reaction at low temperatures [16]. A synergism of redox and acidity of Ce-based catalysts doped by W or Mo was considered to be critical in NH_3 -SCR. As known, the chlorinated alkane could be activated on hydroxyl group to form reactive alkoxy at low temperature [17,18]. Mo species on the surface could often promote the formation of Brönsted acid sites (H^+) through acidic Mo-OH [19]. Additionally, it was found that water dissociation could be promoted by Mo addition into FeOCl catalyst [20]. Surface oxygen from CeO_2 domain increases the possibility of water dissociation, promoting dynamically the formation of Brönsted acid and hydroxyl group, which are favorable for Cl removal. Thus, there would be a chance to develop highly effective $\text{MoO}_x/\text{CeO}_2$ catalysts in catalytic combustion of CVOCs. In this work, $\text{MoO}_x/\text{CeO}_2$ catalysts with Mo loading in a range of 0.9–12.0 wt% were prepared by wet impregnation with $(\text{NH}_4)_6\text{H}_8\text{Mo}_7\text{O}_{28}$ aqueous solution and investigated in catalytic combustion of 1,2-DCE and other CVOCs. The relations of surface performance of as-synthesized catalysts to their activity, selectivity and stability were investigated.

2. Experimental

2.1. Catalyst preparation

80 mL deionized water solution containing 20 g $\text{Ce}(\text{NO}_3)_3 \cdot 6 \text{H}_2\text{O}$ and 6 g $\text{CH}_4\text{N}_2\text{O}$ was placed into autoclave and then heated at 140 °C for 300 min. The precipitate was washed with deionized water, then treated thermally at 110 °C overnight, and finally calcined at 450 °C in air for 4 h. As-synthesized CeO_2 was impregnated by wet impregnation with a given amount of $(\text{NH}_4)_6\text{H}_8\text{Mo}_7\text{O}_{28}$ aqueous solution, and then thermally treated with the same procedure as that for CeO_2 . Mo loadings of the obtained samples were in a range of 0.9–12.0 wt%. $\text{MoO}_x/\text{CeO}_2$ samples were denoted as yMo, where y is Mo density in a range of 0.6–13.0 Mo atom nm^{-2} . For example, Mo density of 0.6Mo sample was 0.6 Mo atom nm^{-2} .

2.2. Catalyst characterization

The characterization methods of as-synthesized $\text{MoO}_x/\text{CeO}_2$ catalysts by XRD, Raman, XPS, H_2 -TPR, O_2 -TPD, CO_2 -TPD, Py-FT-IR and DRIFTS were previously described in our published paper [8,9,21] (Supporting information).

2.3. Catalyst activity measurement

The activity, selectivity and stability of $\text{MoO}_x/\text{CeO}_2$ catalysts for combustive oxidation of CVOCs were investigated in a reactor (4 mm diameter) made of quartz. The mixture of 100 mg grain catalyst (40–60 mesh) and 100 mg quartz-particle with the same size was placed in the reactor bed, through which the feed composed of 10% O_2/N_2 containing 1000 ppm reactant flowed at 100 mL min^{-1} , where gas hour space velocity (GHSV) is 60,000 h^{-1} . The reaction temperatures were controlled at 100–500 °C. On-line analyses for organic compounds were conducted with GC (GC9790, FULI) equipped with a flame ionization detector (FID) and a KB-5–30 m × 0.32 mm × 0.50 μm capillary column. Considering negligible change in feed volume, the conversion was calculated by the difference between initial and final reactant concentrations divided by initial reactant concentration. The effluent stream bubbled through 0.0125 N NaOH solution to absorb HCl and Cl_2 . The amount of Cl_2 was determined by titrating the solution saturating Cl_2 with ferrous ammonium sulphate using N,N-diethyl-p-phenylenediamine as an indicator [22].

2.4. In situ FTIR

Nicolet 6700 FTIR equipped with liquid nitrogen cooled mercury-cadmium-telluride detector was applied to conduct in situ diffuse

reflectance infrared Fourier transform spectroscopy (DRIFTS) experiments. DRIFTS cell (Harrick, HVC-DRP) fitted with ZnSe window was used as the reaction chamber that allowed samples to be heated to 650 °C, and the spectra were recorded within a frequency range of 4000–1000 cm^{-1} at the resolution of 4 cm^{-1} and 64 scans. 80 mg grain catalyst (40–60 mesh) was packed in DRIFTS cell. For 1,2-DCE adsorption spectra, the samples were pretreated at 400 °C by flowing 10% O_2/Ar flow for 60 min with subsequent exposure to 1000 ppm 1,2-DCE/Ar feed to saturation at various temperatures, then to Ar for 30 min, and FT-IR spectra were finally recorded. For 1,2-DCE oxidation spectra, the sample was pretreated at 400 °C by flowing 20% O_2/Ar for 2 h with subsequent exposure to 1000 ppm 1,2-DCE balanced with 20% O_2/Ar at various temperatures. Then the sample was purged with 20% O_2/Ar for 30 min and the corresponding spectrum was recorded.

3. Results and discussions

3.1. Catalyst characterization

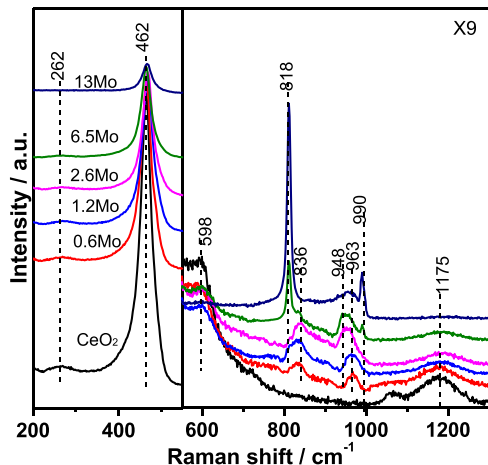
3.1.1. Physical properties

Mo contents of $\text{MoO}_x/\text{CeO}_2$ samples are determined by ICP-AES to be 0.9–12.0 wt% (Mo density, 0.6–13.0 Mo atom nm^{-2} (Table 1)). N_2 adsorption and desorption isotherms (Fig. S1) exhibit regularly stacking tubular pores, whose size is estimated by BJH model from the desorption isotherm branch to be 7.9–3.8 nm, decreasing with Mo loading. Correspondingly, the surface area estimated by BET model from the adsorption isotherm branch decreases from 102 to 58 $\text{m}^2 \text{g}^{-1}$, which is consistent with the decrease of pore volume, due to the coverage of MoO_x over CeO_2 . On XRD patterns (Fig. S2), the diffraction peaks appear at 28.6, 33.2, 47.4, 56.4 and 59.1°, ascribed to the reflections from cubic fluorite CeO_2 (JCPDS No. 34–0394). The peaks at 12.8, 23.3, 25.7 and 27.3°, assigned to crystal MoO_3 (JCPDS No. 35–0609), are observed only for 13Mo sample. Almost no significant shifts of main reflection from (111) plane of CeO_2 are observed (in the enlarged 26–32° section, Fig. S2), and the lattice parameters is $0.5409 \pm 0.0003 \text{ nm}$ (Table 1). It can be considered that Mo entrance into cubic fluorite CeO_2 may be difficult under experimental condition. As confirmed by X-ray absorption spectra, 4.6 Mo atom nm^{-2} on Al_2O_3 surface reached a monolayer of MoO_x [23]. XRD results support that highly dispersed Mo species exists on the surface of 0.6Mo, 1.2Mo and 2.6Mo samples with Mo sub-monolayer structure.

On Raman spectrum (Fig. 1) of CeO_2 , $\text{F}2\text{g}$ mode of fluorite phase at 462 cm^{-1} is dominant, while 2TA, D and 2LO modes at 262, 598, and 1175 cm^{-1} become weak [24]. The $\nu_{\text{F}2\text{g}}$ band is ascribed to lattice oxygen vibrations, which is sensitive to crystalline symmetry. In the cases of CeO_2 doped with the second element, such as W and Ti, it becomes broad and weak [21,25], really due to the distortion of CeO_2 lattice through the interaction between CeO_2 and the doped element. It was found that the oxygen sublattice was significantly distorted during loading the second metal element, leading to destabilization of oxide ions in terms of modification in Ce-O length [26]. With Mo loading, Ce-O bond becomes weak and long near a Mo-atom placed on CeO_2 surface. For 13Mo sample, the local lattice structure of CeO_2 can be significantly disordered due to MoO_x excessive coverage, which leads to the decrease in the intensity of $\nu_{\text{F}2\text{g}}$ band, as WO_x/CeO_2 did [21]. The bands at 599 and 1175 cm^{-1} are ascribed to oxygen vacancy and superoxo species (O_2^-) on CeO_2 domain, respectively [24], which become weak gradually with Mo loading, and finally disappear at 13Mo atom nm^{-2} . The structural information of MoO_x under dehydrated condition is also available in Fig. 1. There appear the bands at 963 and/or 948 cm^{-1} , which are assigned to the terminal Mo=O bond stretching mode of the isolated monomolybdate dioxo MoO_4 ($(\text{O}=\text{)}_2\text{Mo}(\text{O-Ce})_2$) [27,28], where one Mo atom bonds two Ce atoms. The band appearing at 836 cm^{-1} temporarily is ascribed to Mo-O-Ce. For $\text{MoO}_x/\text{Al}_2\text{O}_3$ and $\text{MoO}_x/\text{ZrO}_2$, the bands related to Mo-O-Al and Mo-O-Zr appeared at 838 and 845 cm^{-1} [29], respectively. Generally, dioxo MoO_4 structures give rise to

Table 1The structure and physical parameters of $\text{MoO}_x/\text{CeO}_2$ samples.

Sample	$S_{\text{BET}} / \text{m}^2 \text{g}^{-1}$	$V_{\text{pore}} / \text{cm}^3 \text{g}^{-1}$	$D_{\text{pore}} / \text{nm}$	Mo Loading ^a / wt%	Mo density / atom nm^{-2}	L^b / nm^c	Mo species under dehydrated condition ^c	Mo species under humid condition ^c
CeO_2	102	0.070	3.8	–	0	0.5407	–	–
0.6Mo	100	0.070	3.8	0.9	0.6	0.5409	$(\text{O}=\text{)}_2\text{Mo}(\text{O-Ce})_2$	$[\text{MoO}_4]^{2-}$
1.2Mo	97	0.069	3.9	1.8	1.2	0.5410	$(\text{O}=\text{)}_2\text{Mo}(\text{O-Ce})_2$	$[\text{MoO}_4]^{2-}$
2.6Mo	90	0.065	4.0	3.8	2.6	0.5412	$(\text{O}=\text{)}_2\text{Mo}(\text{O-Ce})_2$	$[\text{MoO}_4]^{2-} + [\text{Mo}_7\text{O}_{24}]^{6-}$
6.5Mo	71	0.058	5.7	7.4	6.5	0.5406	$(\text{O}=\text{)}_2\text{Mo}(\text{O-Ce})_2$ oligomer MoO_4 nano-particles	$[\text{Mo}_7\text{O}_{24}]^{6-}$ nano-particles
13Mo	58	0.049	7.9	12	13	0.5406	oligomer MoO_4 nano-particles	$[\text{Mo}_7\text{O}_{24}]^{6-}$ nano-particles

^a Determined by ICP-AES;^b lattice parameters;^c identified by Raman.**Fig. 1.** The Raman spectra of $\text{MoO}_x/\text{CeO}_2$ samples under dehydrated conditions as the function of Mo loading.

both Vs and V_{as} bands that are separated by about $10 - 30 \text{ cm}^{-1}$. MoO_x primarily contained dioxo MoO_4 structures on SiO_2 ($(\text{O}=\text{)}_2\text{Mo}(\text{O-Si})_2$), when Mo content was below 5% [27]. At 6.5 Mo atom nm^{-2} or higher, new bands appear at 818 and 990 cm^{-1} , which are assigned to Mo-O-Mo, due probably to the formation of oligomer dioxo MoO_4 species (in which Mo substitutes the site of Ce of $(\text{O}=\text{)}_2\text{Mo}(\text{O-Ce})_2$, and each Mo atom combines with four oxygen atoms) or MoO_3 nanoparticles [30], consistent with XRD result. The band at 836 cm^{-1} becomes significantly weak, because the formation of oligomer monomolybdate MoO_4 or nanoparticles results in the decrease in Mo-O-Ce. Under humid condition, F2g mode of CeO_2 fluorite phase shifts to 456 cm^{-1} , and the band ascribed to Mo-O-Ce species appears at $773 - 824 \text{ cm}^{-1}$ (Fig. S3). For 0.6Mo and 1.2Mo samples, the bands at 857 and 911 cm^{-1} are well consistent with Raman bands of the aqueous $[\text{MoO}_4]^{2-}$ anion (isolated tetrahedral sites) [31]. Increasing Mo density to 2.6 Mo atom nm^{-2} , slight shift of the highest frequency band from 911 to 940 cm^{-1} ascribed to the vibration of Mo=O is probably related to the distortion of the hydrated, isolated $[\text{MoO}_4]^{2-}$ anion on the CeO_2 surface as well as minor amounts of $[\text{Mo}_7\text{O}_{24}]^{6-}$ anions (oligomeric octahedral clusters). The vibrations from bridging Mo-O-Mo bond at 808 cm^{-1} is not significant at 2.6 Mo atom nm^{-2} or lower. For 6.5Mo and 13Mo samples, the band of Mo=O shifts to 950 cm^{-1} , probably due to the formation of $[\text{Mo}_7\text{O}_{24}]^{6-}$ clusters. The bands appearing within $659 - 808 \text{ cm}^{-1}$ closely match the vibrations of Mo-O-Mo bonds in the aqueous $[\text{Mo}_7\text{O}_{24}]^{6-}$ clusters. The positive ions marching anions can be either $\text{Ce}^{4+}/\text{Ce}^{3+}$ ions or protons.

3.1.2. Chemical states and redox of catalysts

Fig. 2 exhibits XPS spectra of Mo 3d, O 1s and Ce 3d electronic levels for $\text{MoO}_x/\text{CeO}_2$ samples. For Mo 3d, the binding energies (BE) of Mo 3d_{5/2} and 3d_{5/2} are $235.6 - 235.8 \text{ eV}$ and $323.4 - 323.6 \text{ eV}$, respectively

[23], identifying that Mo species exists mainly in a form of Mo^{6+} , whose chemical valance matches with Mo species in $(\text{O}=\text{)}_2\text{Mo}(\text{O-Ce})_2$, oligomer dioxo MoO_4 structure and MoO_3 particles. Additionally, very weak peaks at 235.0 eV and $231.5 - 231.7 \text{ eV}$ on Mo 3d spectra were obtained (the enlarged spectra shown in Fig. S4), which should be ascribed to Mo^{5+} species [32], probably due to x-ray irradiation. This effect is weak, probably because of strong interaction between MoO_x and CeO_2 through the formation of Mo-O-Ce, especially for highly dispersed Mo on the surface. On O 1s spectra, it is identified by deconvolution that there two kinds of oxygen species, lattice oxygen (O_{latt}) and surface oxygen (O_{sur}), whose BE are $529.4 - 529.8$ and 531.1 eV , respectively. BE of O_{latt} for 0.6Mo, 1.2Mo and 2.6Mo samples is in a range of $529.4 - 529.5 \text{ eV}$, similar to that of CeO_2 , 529.4 eV . 6.5Mo and 13Mo samples show the increased O_{latt} BE. The ratio of $\text{O}_{\text{sur}}/\text{O}_{\text{total}}$ decreases with Mo loading (Table 2). As known, there exist surface oxygen species such as O_2^{2-} , O_2^- , O^- and hydroxyl group on CeO_2 surface. On Ce 3d spectra, the identified peaks with deconvolution method are caused by the pairs of spin orbit doublets. Ce^{4+} contributes to six peaks denoted as v, v', v'', u, u', u'', and Ce^{3+} , to peaks as v', u'. The Ce^{3+}/Ce ratio is almost not modified by Mo.

The reducibility of $\text{MoO}_x/\text{CeO}_2$ samples was investigated by H_2 -TPR tests (Fig. 3 A). All samples were pretreated in Ar flow at $450 \text{ }^\circ\text{C}$ for 2 h, and thus the reduction of surface oxygen species cannot be considered. For CeO_2 sample, a broad flat peak appearing in a range of $275 - 552 \text{ }^\circ\text{C}$ is divided by deconvolution into two peaks, which can be ascribed to the reduction of surface Ce^{4+} species on small or highly defective nanoparticles (low temperature peak) and on large CeO_2 particles (high temperature peak), respectively. For the samples with Mo density below 2.6 Mo atom nm^{-2} , the initial reduction temperature is $275 \text{ }^\circ\text{C}$, almost similar to that for CeO_2 sample. While the initial reaction of 6.5Mo and 13Mo samples shifts to high temperature, indicating that MoO_x interacts preferentially with basic lattice oxygen on large CeO_2 particles, whose decrease is confirmed by CO_2 -TPD result (Fig. S5). In fact, the peak at low temperature disappears on 6.5Mo and 13Mo samples, suggesting that there is no exposed Ce^{4+} species on defective sites, over which Mo-O-Mo covers. This phenomenon is different from the case of WO_x/CeO_2 [21] and CuO-CeO_2 [33], where the doping metal anchored on defective sites. The second peak ending at $552 \text{ }^\circ\text{C}$ on 0.6Mo, 1.2Mo and 2.6Mo samples can be ascribed to the reduction of Mo-O-Ce and the exposed Ce^{4+} on large CeO_2 particles, and becomes strong with the increase in Mo-O-Ce. There appears a new peak at $500 \text{ }^\circ\text{C}$ on 2.6Mo, 6.5Mo and 13Mo samples with the intensity order of $6.5\text{Mo} > 13\text{Mo} > 2.6\text{Mo}$, which should be related to the reduction of oligomer dioxo MoO_4 . The theoretical H_2 consumption is calculated to be $1.13 - 1.84 \text{ mmol g}^{-1}$ (Table 2) based both on the normalized reduction of Ce^{4+} by surface area and Ce^{4+} composition (XPS data) and on the reduction of Mo^{6+} to Mo^{4+} (Table S1). The experimental H_2 consumption is $1.14 - 1.77 \text{ mmol g}^{-1}$, only with small differences compared with the calculated values, confirming that Mo^{6+} is reduced at the same time as the reduction of Ce^{4+} . For 13 Mo sample with the increased Mo-O-Mo, the peak staring at $610 \text{ }^\circ\text{C}$ can be assigned to the reduction of MoO_x

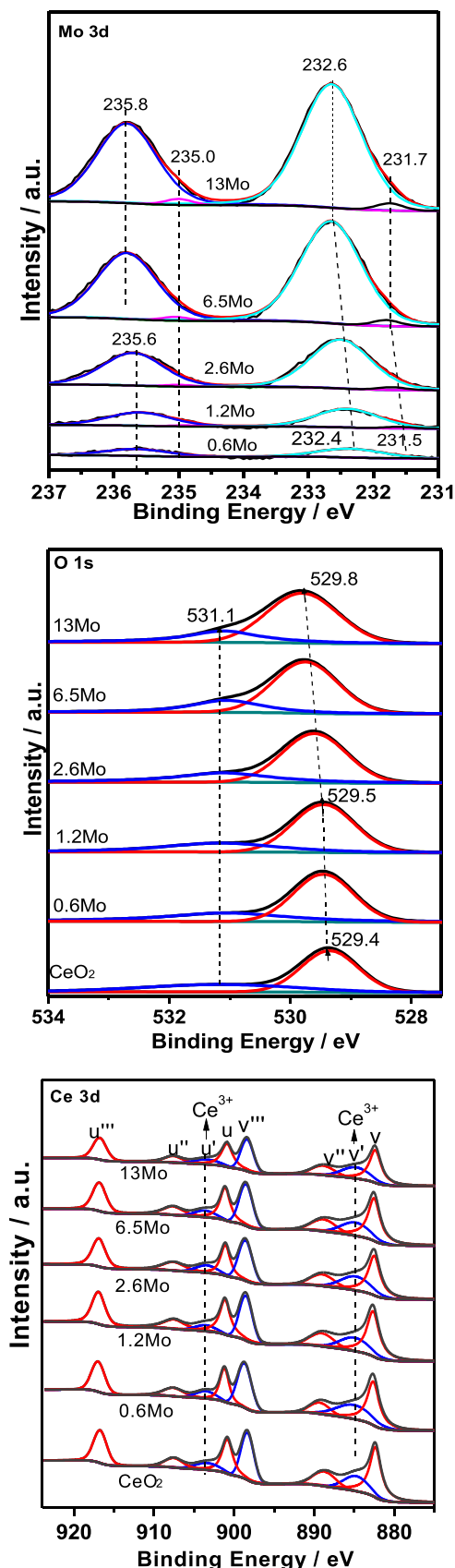


Fig. 2. The XPS spectra of O 1 s, Mo 3d and Ce 3d for $\text{MoO}_x/\text{CeO}_2$ samples.

particles, which is similar to the reduction profiles of MoO_3 (Fig. S6). Obviously, the reducibility of Mo^{6+} in $(\text{O}=\text{)}_2\text{Mo}(\text{O}-\text{Ce})_2$ species can be promoted through the interaction between Ce and Mo species.

Fig. 3B shows O_2 -TPD profiles of $\text{MoO}_x/\text{CeO}_2$ samples. Generally, O_2 desorption follows as physically adsorbed O_2 , reversibly and chemically adsorbed O_2^{2-} , irreversibly and chemically adsorbed O_2^- , surface O^- species and lattice O^{2-} species. The O_2 -TPD profile of CeO_2 sample is identified by deconvolution as four desorption peaks with the maxima at 260, 357, 460 and 600 °C, which are generally assigned to the desorption of O_2^{2-} , O_2^- , O^- and O^{2-} , respectively. The peroxide (O_2^{2-}) species and superoxide (O_2^-) are Raman-active [34,35], and are observed at 820 – 836 and 1175 cm^{-1} on Raman spectra of CeO_2 , 1.2Mo and 2.6Mo (as respective samples) treated under the similar condition to that for O_2 -TPD tests (Fig. S7). The desorption of O_2^{2-} species becomes strong with Mo loading (Fig. 3 C), probably because Mo contacted with CeO_2 domain promotes the formation of O_2^{2-} , similar to the case of WO_x/CeO_2 with 5.2 W atom nm^{-2} pretreated with He before exposure to O_2 [36]. For 6.5Mo and 13Mo samples, O_2^{2-} species decreases quickly. At the same time, the desorption of O_2^- and O^- decreases gradually (Fig. 3 C), and almost disappears on the profile of 13 Mo sample. Generally, the dissociation of O_2^{2-} adsorbed on CeO_2 domain to O^- occurs significantly. These results indicate that O_2^{2-} , O_2^- and O^- species are mainly from the exposed CeO_2 . The desorption of weak surface lattice oxygen at 500 – 700 °C from the 0.6Mo, 1.2Mo and 2.6Mo samples decreases, due to MoO_4 anchoring on surface lattice oxygen, which is confirmed by CO_2 -TPD tests, where the surface basic lattice oxygen is inversely to Mo density (Fig. S5). For $\text{MoO}_x/\text{Al}_2\text{O}_3$ catalysts, isolated dioxo MoO_4 anchored on basic Al-OH [37]. The desorption of surface lattice oxygen from 6.5Mo and 13Mo samples becomes strong, which should be related to MoO_x nano-particles.

3.1.3. Acidity

FT-IR spectra of pyridine adsorption on $\text{MoO}_x/\text{CeO}_2$ samples at 200 °C are shown in Fig. 4A. A band appearing at 1440 cm^{-1} is related to pyridine adsorption on Lewis acid. The amount and density of Lewis acid is estimated based on sample mass, surface area and thickness of the solid wafer, concentration of pyridine adsorbed on the sample wafer (Table S2). CeO_2 presents very weak band at 1440 cm^{-1} with Lewis acid amount of 0.45 umol m^{-2} . For the samples with isolated $(\text{O}=\text{)}_2\text{Mo}(\text{O}-\text{Ce})_2$ structure, The band at 1440 cm^{-1} becomes strong with Mo loading. The corresponding Lewis acid density is directly proportional to Mo density (Fig. 4B). 2.6Mo sample presents the largest Lewis acidity, 15.9 umol m^{-2} . For 6.5Mo and 13Mo samples with the decreased $(\text{O}=\text{)}_2\text{Mo}(\text{O}-\text{Ce})_2$ structure, the band at 1440 cm^{-1} becomes much weaker, and Lewis acid density is 2.4 and 1.0 umol m^{-2} . Obviously, the metal ions of $(\text{O}=\text{)}_2\text{Mo}(\text{O}-\text{Ce})_2$ structure, $\text{Ce}^{3+}/\text{Ce}^{4+}$ and Mo^{6+} ions, contribute to Lewis acidity. This consideration suggests that the acidity of Mo^{6+} in Mo-O-Mo is poor. Probably, the $(\text{O}=\text{)}_2\text{Mo}(\text{O}-\text{Ce})_2$ contacted with CeO_2 domain promotes the formation of Lewis acid, due to the transfer of electron from Mo^{6+} toward electronically unsaturated surface oxygen. Additionally, Mo-O-Ce leads to the destabilization of oxide ions of CeO_2 in terms of modification in Ce-O length and the increase in defectives of CeO_2 , which promotes the formation of Lewis acid sites ($\text{Ce}^{3+}/\text{Ce}^{4+}$). This phenomenon was observed in the case of CeO_2 doped with Ti, where the defective of CeO_2 increased with the formation of Ce-O-Ti, leading to a great increase in Lewis acidity [25]. Moreover, there appears a very weak band at 1540 cm^{-1} for $\text{MoO}_x/\text{CeO}_2$ samples, indicating the presence of Brønsted acid. As known, some Mo-OH presented Brønsted acid, due to the transfer of electron from OH to Mo=O [19]. Sometimes, water dissociation on Mo species can produce weak Brønsted acid, as Mo heteropoly acid did. 13Mo sample presents almost no band at 1540 cm^{-1} .

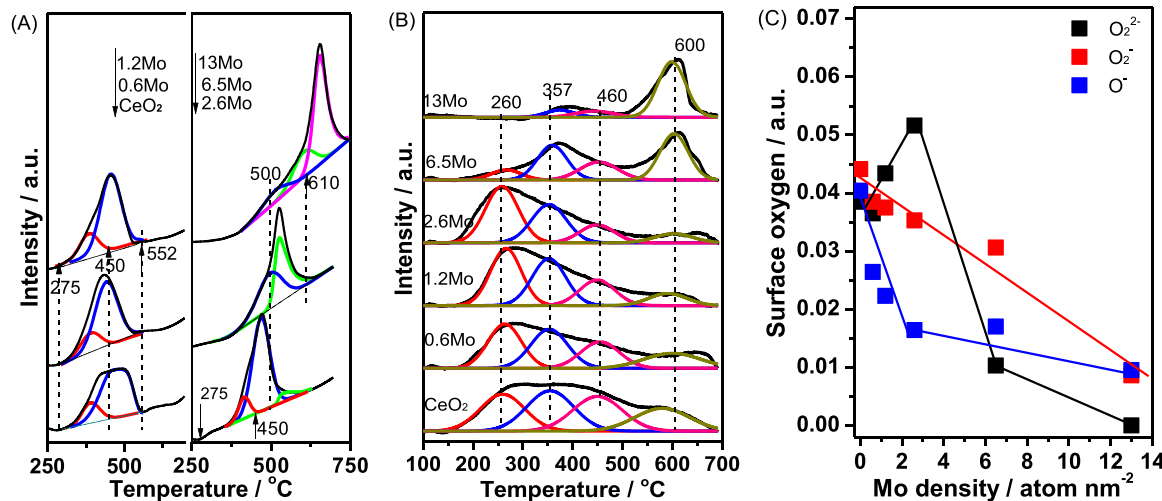
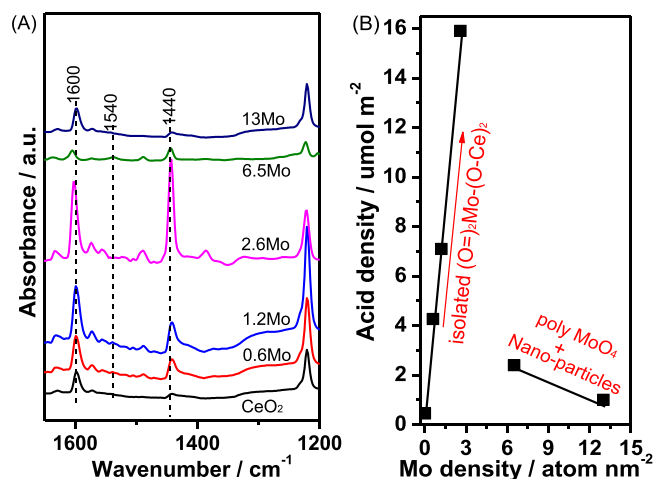
3.2. In situ FT-IR of 1,2-DCE adsorption and oxidation

In situ FT-IR spectra of 1,2-DCE adsorption on CeO_2 , 2.6Mo and

Table 2

XPS data, H₂ consumption and O₂ desorption of MoO_x/CeO₂ samples.

Sample	O _{sur} /O _{total} ^a	H ₂ consumption / mmol g ⁻¹		O ₂ desorption / a.u.			total
		Calculated ^b	experimental	O ₂ ²⁻ (250 °C)	O ₂ ⁻ (350 °C)	O ⁻ (450 °C)	
CeO ₂	0.33	—	1.05	3.93	4.53	4.12	12.58
0.6Mo	0.25	1.13	1.14	3.65	3.85	2.46	9.96
1.2Mo	0.25	1.19	1.08	421	3.46	2.16	9.74
2.6Mo	0.21	1.32	1.23	4.65	3.18	1.48	9.31
6.5Mo	0.21	1.49	1.42	0.75	2.17	1.36	4.28
13Mo	0.20	1.84	1.77	0	0.48	0.55	1.03

^a Estimated by XPS data;^b calculated by Table S1.Fig. 3. The H₂-TPR (A) and O₂-TPD (B) profiles, and surface oxygen (normalized by surface area) vs Mo density (C) of MoO_x/CeO₂ samples.Fig. 4. The Py-FT-IR spectra (A) and acidity vs Mo density (B) for MoO_x/CeO₂ samples.

6.5Mo as the representative samples were shown Fig. 5. On FT-IR spectra (Fig. 5A) of CeO₂ at 200 – 300 °C, strong negative bands with the centers at 3687 – 3546 cm⁻¹ are assigned usually to strong Ce-OH, indicating that the interaction between Ce-OH and 1,2-DCE occurs (Fig. S8A). The bands at 1609 – 1605 cm⁻¹ (Fig. 5A) are ascribed to $\text{vC}=\text{C}$, and the ones at 2337 and 2142 cm⁻¹, to $\text{v}_\text{a}\text{CH}_2$ and $\text{v}_\text{s}\text{CH}_2$ in vinyl species [38]. Generally, HCl can be removed from 1,2-DCE on a pair of acid and base sites to form vinyl chloride (VC). There appears a band at 1650 – 1620 cm⁻¹, accompanied by a band at 1419 cm⁻¹. Combining the appearance of $\text{vC}=\text{C}$ species, these bands can be

attributed to a surface enolic species. One evidence is that the IR spectra of syn-vinyl alcohol ($\text{CH}_2=\text{CHOH}$) in gas phase, showed strong peak between 1644 and 1648 cm⁻¹, which is accompanied by two peaks at 1409 – 1412 and 1300 – 1326 cm⁻¹ [39]. Additional bands at 1699 – 1678 cm⁻¹ (Fig. 5A), 2934 and 2858 cm⁻¹ (Fig. S8A) corresponding to $\text{vC}=\text{O}$, $\text{v}_\text{s}\text{CH}_2$ and vCH species (acetaldehyde as resonant structure of enolic species [40]) are also present in the spectra of adsorbed 1,2-DCE. Obviously, a part of produced VC adsorbs as enolic structure. At the same time, the bands ascribed to $\text{v}_\text{a}\text{COO}$, $\delta_\text{a}\text{CH}_3$ and δCH_3 in carboxylates with the acetate type appear at 1543 – 1556, 1432 and 1361 cm⁻¹, respectively [41]. Raising the temperature to 350 °C or higher, the bands related to intermediates containing oxygen become weak, indicating that surface oxygen is involved in further oxidation. According to the fact that the activity of CeO₂ for parallel oxidations of VC and 1,2-DCE is similar (Fig. S9), it can be considered that the reaction mainly follows the pathway of 1,2-DCE → VC → -O-CH=CH₂ → -acetate → -COx. With Mo addition, no bands related to vinyl species are observed. The negative bands in the section of hydroxyl group become very weak, while the band appearing at 1696 – 1684 cm⁻¹ becomes strong at 150 °C (Fig. 5B), accompanying with weak bands at 2957, 2136 (Fig. S10A) and 1307 cm⁻¹, which can be ascribed to acetyl species [42]. This phenomenon indicates that -O-CH₂-CH₂⁺ species resulted from the abstraction of Cl on strong Mo⁶⁺ Lewis acid site and then the combination between carbonium and basic lattice oxygen near Mo⁶⁺=O species can be transformed readily into acetyl species. Raising temperature, the bands to acetyl species becomes gradually weak, while further oxidation products, such as acetate (1546, 1505 and 1347 cm⁻¹), acetic acid (1696, 1417 and 1396 cm⁻¹) and carbonate bidentate (1556 and 1373 cm⁻¹) grow in intensities. It can be concluded that the adsorption and activation of 1,2-DCE on 2.6Mo follow the pathway: 1,2-DCE → -O-CH₂CH₂O- → acetyl → acetate or acetic acid →

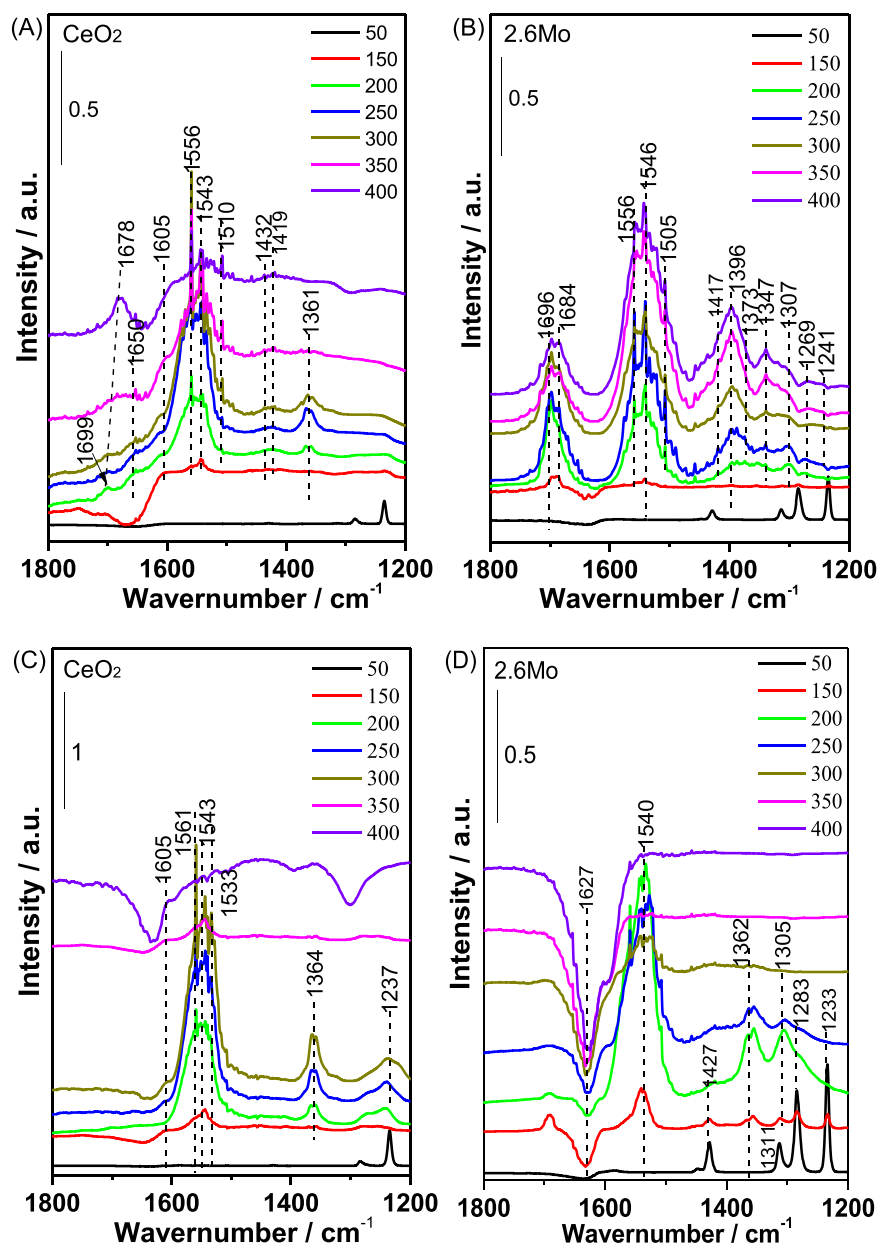


Fig. 5. In situ DRIFT for 1,2-DCE adsorption (A,B) and oxidation (C,D) over CeO_2 (A,C) and 2.6Mo (B,D) samples degassed after the treatment with the stream of 1000 ppm 1,2-DCE in Ar (adsorption) or 20% O_2/Ar (oxidation) from 50 to 400 $^\circ\text{C}$.

carbonate bidentate $\rightarrow \text{CO}_x$. The decreased band intensity on 6.5Mo indicates that active sites for 1,2-DCE adsorption and activation are related to $\text{O}=\text{Mo}-\text{O}-\text{Ce}$ species contacted by CeO_2 domain (Fig. S10B). In the presence of oxygen, the bands over CeO_2 sample related to vinyl species become weak, while the ones to acetate species, strong at various temperatures, suggesting that the oxidation is promoted (Fig. 5C). For 2.6Mo sample, a strong new negative band appears at 1627 cm^{-1} , assigned to hydroxyl in-plane vibration of H_2O (Fig. 5D); a strong broad negative band with the maximum appear at 3296 cm^{-1} (Fig. S10C), assigned to binding hydroxyl vibration of H_2O . Obviously, the consumption of hydroxyl occurs with oxygen presence. The bands at 1396 and 1693 cm^{-1} ascribed to acetic acid disappear. As known, dioxo MoO_4 species is often able for adsorption and dissociation of H_2O molecules on $\text{MoO}_x/\text{Al}_2\text{O}_3$ and $\text{MoO}_x/\text{TiO}_2$ [43,44]. Water loss from $\text{MoO}_x/\text{CeO}_2$ samples is observed up to $700 \text{ }^\circ\text{C}$ by TG (Fig. S11). Water desorption from $\text{Mo}/\text{HZSM-5}$ was observed at $700 \text{ }^\circ\text{C}$, which corresponded to water evolved upon interaction of MoO_3 with the Brønsted acid sites. As

reported, water dissociation on dioxo MoO_4 species was dependent on the electron transfer of surface [20]. The availability of surface oxygen is increased by gas oxygen so that water dissociation can be promoted. On the other hand, the electron transfer from hydroxyl group near oxygen vacancy to surface oxygen is also promoted, and as a result, hydrogen of hydroxyl group becomes effective for combining Cl atom. Probably, high accessibility of hydroxyl group promotes Cl removal as HCl . Indeed, the negative bands in hydroxyl section become stronger, compared with the case without oxygen gas (Fig. S10C). Here, water embodied in MoO_x is consumed through the involvement of hydroxyl group in reaction. Finally, the bands ascribed to intermediates containing oxygen almost disappears below $300 \text{ }^\circ\text{C}$ through their oxidation into CO/CO_2 (CO_x).

3.3. Activity

The catalytic oxidation performance of $\text{MoO}_x/\text{CeO}_2$ catalysts was investigated in 1,2-DCE oxidation as the function of conversion to CO_x at

various temperatures (Fig. 6). The temperature needed for 50% (T_{50}) and 90% (T_{90}) conversion over CeO_2 is 353 and 457 °C, respectively (Table 3). With Mo addition, the conversion curve shifts gradually to low temperature (Fig. 6A). 2.6Mo catalyst with the most $(\text{O}=\text{)}_2\text{Mo} \cdot (\text{O}-\text{Ce})_2$ shows the lowest T_{50} (229 °C) and T_{90} (281 °C), while 13Mo with the most Mo-O-Mo and the least $(\text{O}=\text{)}_2\text{Mo}(\text{O}-\text{Ce})_2$, the highest T_{50} (312 °C) and T_{90} (489 °C) (Fig. 6B). Maintaining the temperature at 250 °C, the conversion over CeO_2 decreases from 50% to 6% within 110 min, which is resulted really from strong adsorption of Cl species produced during the reaction [45] (almost no carbon deposition is observed). The substitution of Cl species for surface oxygen or basic lattice oxygen on the surface of CeO_2 occurs readily, as previously observed in other CVOC's oxidation over CeO_2 [9]. Within 500 min, 0.6Mo, 1.2Mo, 2.6Mo, 6.5Mo and 13Mo catalysts show stable conversion of 52%, 58%, 80%, 35% and 21%, respectively (Fig. 7A). Especially, 2.6Mo was tested under the same condition for another 30 h, and the conversion becomes not significantly changed (Fig. S12). In fact, there is a considerable part of exposed CeO_2 on the surface of 0.6Mo, 1.2Mo and 2.6Mo catalysts with Mo density below a monolayer, where the decrease in conversion should be observed, if the reaction occurred. Obviously, the contribution to conversion is mainly from the reaction on the active sites related to $(\text{O}=\text{)}_2\text{Mo}(\text{O}-\text{Ce})_2$ species. The rates at 200 and 250 °C calculated based on the stable conversion to CO_x are directly proportional to $(\text{O}=\text{)}_2\text{Mo} \cdot (\text{O}-\text{Ce})_2$ (Fig. 7B). In fact, Lewis acidic sites are related to $(\text{O}=\text{)}_2\text{Mo} \cdot (\text{O}-\text{Ce})_2$ species, on which 1,2-DCE is activated to form reactive intermediate, acetyl species. On the other hand, $(\text{O}=\text{)}_2\text{Mo}(\text{O}-\text{Ce})_2$ species can promote the dissociation of water produced during the reaction to form proton and hydroxyl, which are favorable for the removal of Cl species produced during the reaction as HCl , and thus inhibits Cl adsorption. Because stable conversion over CeO_2 below 250 °C is very low, TOF_{Mo} estimated based on the stable conversion to CO_x at 200 and 250 °C per Mo atom per second vs Mo density of 0.6Mo, 1.2Mo and 2.6Mo catalysts can be used to investigate the effect of CeO_2 domain on the activity of $(\text{O}=\text{)}_2\text{Mo}(\text{O}-\text{Ce})_2$ species. As shown in Fig. 7C, TOF_{Mo} decreases with Mo density, and is directly proportional to the surface oxygen normalized by Mo content, suggesting that $(\text{O}=\text{)}_2\text{Mo}(\text{O}-\text{Ce})_2$ species rounded by more Ce species is more active. The TOF_{Mo} for 0.6Mo catalyst reaches the highest, $1.6 \times 10^{-3} \text{ s}^{-1}$, and for 2.6Mo catalyst, decreases down to $0.74 \times 10^{-3} \text{ s}^{-1}$. In another experiment, each 0.5 g 1–10 μm powder CeO_2 and 2.6Mo or 6.5Mo are mixed completely and contacted closely under 20 MPa to prepare physically close mixture catalysts noted as 0.5–2.6Mo+0.5–CeO₂ and 0.5–6.5Mo+0.5–CeO₂ (Fig. S13A), over which the TOF_{Mo} at 250 °C is 1.07 and $0.38 \times 10^{-3} \text{ s}^{-1}$, respectively, higher than their arithmetic mean (0.71 and $0.18 \times 10^{-3} \text{ s}^{-1}$) (Table S3). The relation between TOF_{Mo} and Mo density or surface

Table 3

The activity data of $\text{MoO}_x/\text{CeO}_2$ catalysts for 1,2-DCE combustion.

catalysts	T_{50} / °C	T_{90} / °C	Rate / $\mu\text{mol min}^{-1} \text{m}^{-2}$	$\text{TOF}_{\text{Mo}} \times 10^{-3} / \text{s}^{-1}$	$\text{Ea} / \text{kJ mol}^{-1}$
CeO_2	353 (413) ^a	457 (–)	0.03(0.017)	–	57
0.6Mo	247	323	0.12	1.62	43
1.2Mo	240	296	0.13	0.99	37
2.6Mo	229 (260)	281 (320)	0.20 (0.11)	0.70 (0.37)	29
6.5Mo	268	345	0.11	0.16	44
13Mo	312	> 450	0.09	0.06	47

^a The values within parentheses are obtained in wet feed.

oxygen is similar to that for $\text{MoO}_x/\text{CeO}_2$ catalysts (Fig. 7C). Moreover, the selectivity for VC is similar to those for the catalysts containing similar Mo amount, 1.2Mo and 2.6Mo catalysts (Fig. S13B and S13C). Here, it is reasonable to deduce that the interaction between mono dioxo MoO_4 on CeO_2 and basic sites on CeO_2 domain occurs, which inhibits the formation of VC, and promotes the activity of $(\text{O}=\text{)}_2\text{Mo}(\text{O}-\text{Ce})_2$ through the increase in availability of surface oxygen from CeO_2 domain. Decreasing oxygen concentration ($[\text{O}_2]$) from 10% to 2.5% with maintaining 1,2-DCE concentration ([1,2-DCE]) at 1000 ppm, the conversion at high temperature over CeO_2 quickly decreases, down to 10% at 400 °C (Fig. 8A). The conversion curves over 1.2Mo and 2.6Mo shift high temperature to a slight extent (Figs. 8B and 8C), while 13Mo becomes significantly less active (Fig. S14A). This phenomenon confirms that the oxygen vacancy contacted with $(\text{O}=\text{)}_2\text{Mo}(\text{O}-\text{Ce})_2$ is more accessible for oxygen molecules, due to Cl removal. On the other hand, increasing [1,2-DCE] up to 2000 ppm at 10% $[\text{O}_2]$, the rate over 1.2Mo and 2.6Mo is as two times as those obtained at 1000 ppm [1,2-DCE] (Figs. 8E and 8F), suggesting that the increase in the amount of Cl produced during the reaction cannot decrease the availability of surface oxygen on CeO_2 contacted with $(\text{O}=\text{)}_2\text{Mo}(\text{O}-\text{Ce})_2$. In other words, active oxygen on the surface of catalysts with $(\text{O}=\text{)}_2\text{Mo}(\text{O}-\text{Ce})_2$ is highly resistant to Cl substitution. For 13Mo, the rate increases by about 1.4 times (Fig. S14B), indicating that the dependency of reaction on [1,2-DCE] is below the first order without enough surface oxygen.

The apparent activation energy (Ea) for 1,2-DCE oxidation is estimated (Fig. S15) to be 57 kJ mol^{-1} for the fresh CeO_2 (Table 3). According to the in situ FT-IR results, a considerable part of 1,2-DCE is transformed over CeO_2 into VC. Ea for VC oxidation over CeO_2 is 64 kJ mol^{-1} , similar to that for 1,2-DCE. If VC is formed, the abstraction of Cl from Cl-C is difficult, due to the conjugation of Cl p-orbital with $\text{C}=\text{C}$ π -orbital. And strong Cl adsorption on CeO_2 also leads to high Ea . Generally, Cl produced during the reaction was removed from CeO_2 .

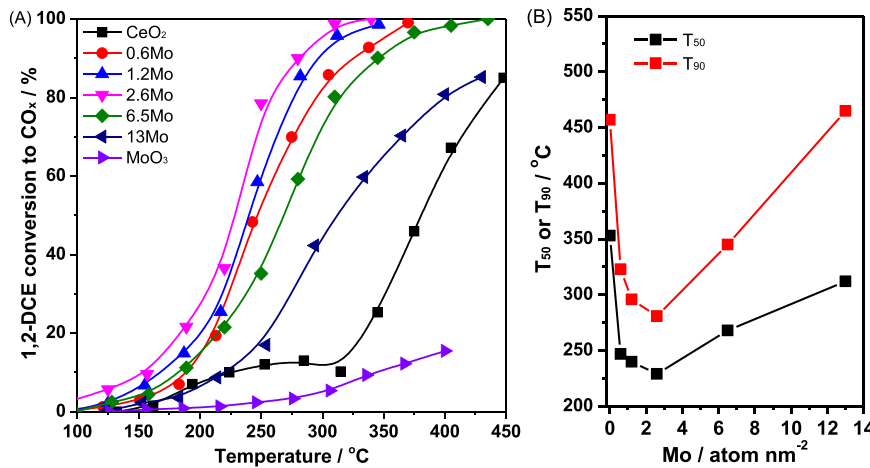


Fig. 6. The 1,2-DCE conversion curves on $\text{MoO}_x/\text{CeO}_2$ catalysts (A), and T_{50} and T_{90} vs Mo density (B); gas composition: 1000 ppm 1,2-DCE, 10% O_2 and N_2 balance; GHSV = 60,000 h^{-1} ; catalyst amount: 100 mg.

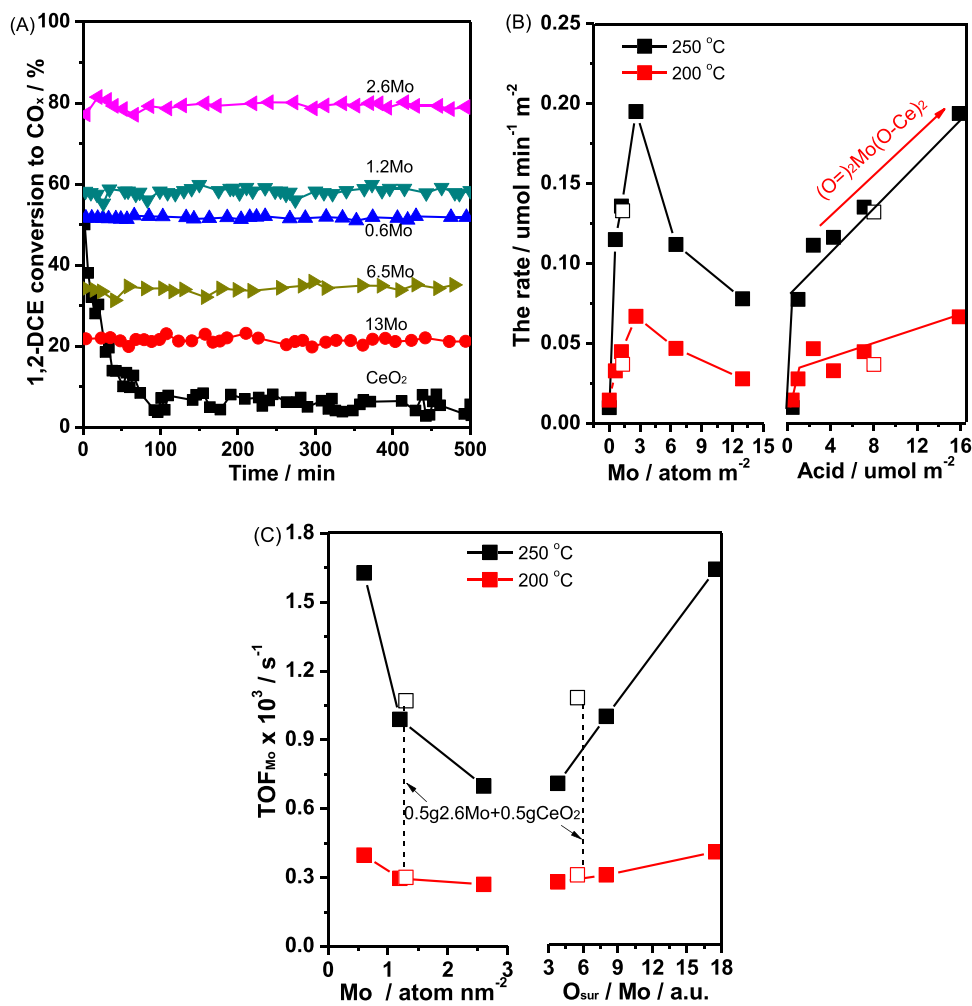


Fig. 7. The stability of $\text{MoO}_x/\text{CeO}_2$ catalysts on 1,2-DCE stream at $250\text{ }^\circ\text{C}$ (A), the stable rate vs Mo density and acid density (B) and the TOF_{Mo} vs Mo density and surface oxygen normalized by Mo amount (C); solid symbol: $\text{MoO}_x/\text{CeO}_2$ catalysts, hollow symbol: physically close mixture catalysts; gas composition: 1000 ppm 1,2-DCE, 10% O_2 and N_2 balance; GHSV = 60,000 h^{-1} ; catalyst amount: 100 mg.

through Deacon ($\text{HCl} + \text{O}_2 \rightarrow \text{Cl}_2 + \text{H}_2\text{O}$) with E_a of $70 - 90\text{ kJ mol}^{-1}$, which becomes significant at $320\text{ }^\circ\text{C}$ or higher [11]. $\text{MoO}_x/\text{CeO}_2$ catalysts present E_a values in a range of $29 - 47\text{ kJ mol}^{-1}$. As known, the abstraction of two Cl atom from 1,2-DCE can be carried out on the adjacent two strong Lewis acidic sites to form reactive $-\text{O}-\text{CH}_2-\text{CH}_2-\text{O}-$ species or acetyl, which are the precursors of acetate species, as observed with in situ FT-IR. The promoted proton H^+ and hydroxyl group by water dissociation on $(\text{O}=\text{)}_2\text{Mo}(\text{O}-\text{Ce})_2$ are both responsible for Cl removal as HCl . Therefore, it can be concluded that the activity order for 1,2-DCE oxidation of MoO_x species supported on CeO_2 follows as $(\text{O}=\text{)}_2\text{Mo}(\text{O}-\text{Ce})_2 > \text{oligomer MoO}_4 > \text{MoO}_x$ particles. High activity of $\text{MoO}_x/\text{CeO}_2$ catalysts with $(\text{O}=\text{)}_2\text{Mo}(\text{O}-\text{Ce})_2$ can be ascribed to a synergism of strong Lewis acidity, high availability of surface oxygen and resistance to Cl poisoning. The decrease in activity of oligomer dioxo MoO_4 and MoO_3 particles is resulted from less acidity, less reducibility and low ability for water dissociation. Additionally, for the oxidation of other CVOCs, such as trichloroethylene, chlorobenzene and 1,2-dichlorobenzene, 2.6Mo shows high activity and selectivity for CO_x and HCl , with E_a of $74, 47$ and 47 kJ mol^{-1} and with T_{90} of $320, 335$ and $350\text{ }^\circ\text{C}$, respectively, in the feed composed of 1000 ppm reactant and 10% O_2 at $\text{GHSV} = 60,000\text{ h}^{-1}$ (Fig. S16).

3.4. Distribution of products

The products in the effluent for 1,2-DCE oxidation confirmed by

TPSR experiments were analyzed on-line in the parallel kinetic reactions (Fig. 9). Cl_2 is not observed below $280\text{ }^\circ\text{C}$, and after that Cl_2 selectivity increases with temperature (Fig. 9A). As known, Cl_2 is formed through Deacon reaction, for which Ce-based catalysts are highly active [11]. CeO_2 presents 16% Cl_2 selectivity at $400\text{ }^\circ\text{C}$. With Mo addition, Cl_2 selectivity decreases gradually, to 3.0% over 13Mo at $400\text{ }^\circ\text{C}$. A volcanic type function of VC selectivity as temperature is observed over CeO_2 with the highest selectivity of 46% at $280\text{ }^\circ\text{C}$ (Fig. 9B). During the stability test of CeO_2 , VC selectivity increases quickly within 110 min from 10% to 50%, and then slowly to 55% within about 400 min (Fig. S17), indicating that Cl species adsorbed on oxygen vacancy inhibits the VC oxidation, and at the same time probably acts as a base site to abstract hydrogen atom combined with another carbon atom, promoting the formation of VC. Moreover, CeO_2 shows significant selectivity for trichloroethylene and 1,2-dichloroethylene at $300\text{ }^\circ\text{C}$ or higher with the best values of 8% and 33% at $330\text{ }^\circ\text{C}$, respectively (Fig. 9B). Probably, the chlorination products, such as 1,1,2-trichloro- ethane and 1,1,2,2-terachloroethane, are their precursors. With the decrease in $[\text{O}_2]$ from 10% to 2.5%, the amount of trichloroethylene and dichloroethylene significantly increases (Fig. S18), indicating that the chlorination becomes strong. According to the fact that the temperature range for chlorination is similar to that for Deacon reaction, it can be considered that Cl_2 is involved in the chlorination. The catalysts with $(\text{O}=\text{)}_2\text{Mo}(\text{O}-\text{Ce})_2$ present a quite similar distribution of VC, where the highest selectivity detected at $300\text{ }^\circ\text{C}$ is below 4%. While VC selectivity

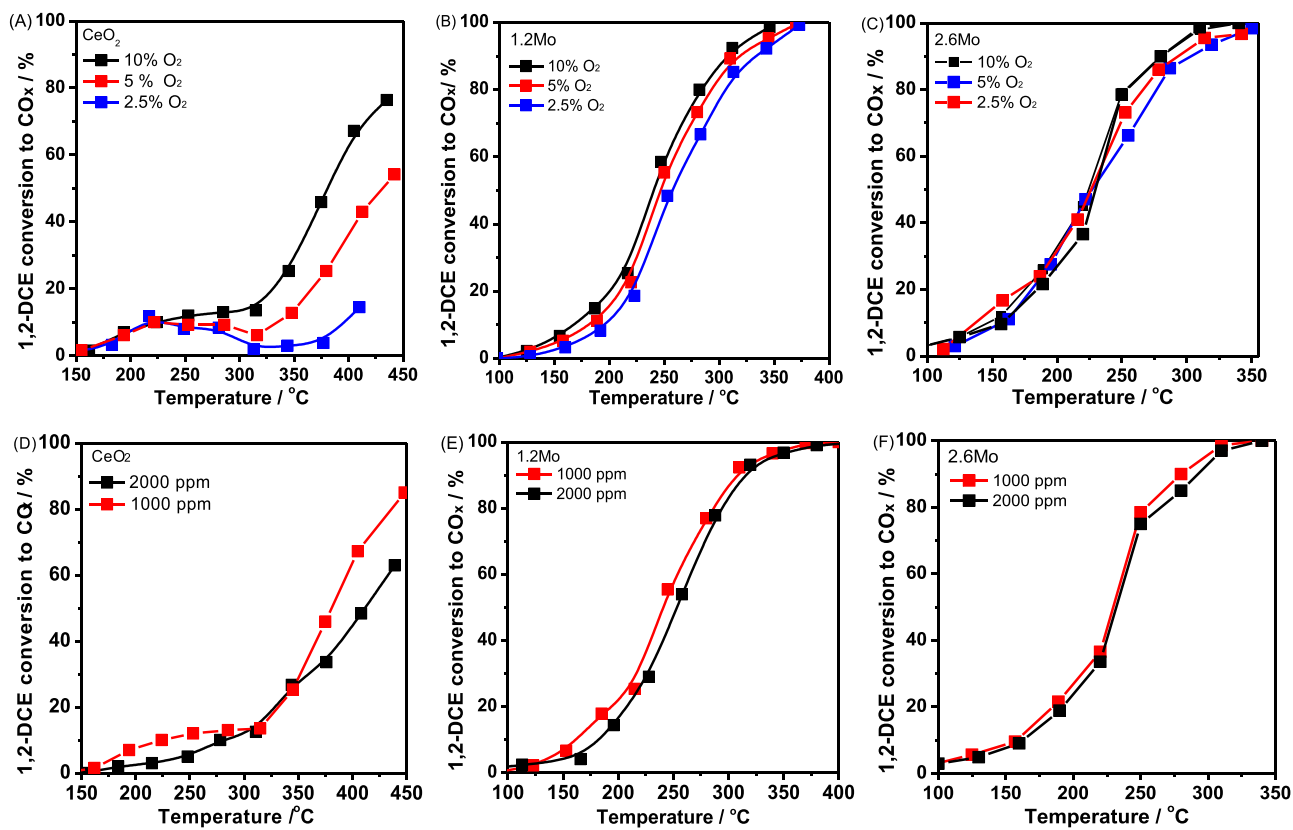


Fig. 8. The conversion curves at 1000 ppm 1,2-DCE and various oxygen concentrations (A, B, C) and at 2000 ppm 1,2-DCE and 10% O₂ (D, E, F) over CeO₂ (A, D), 1.2Mo (B, E) and 2.6Mo (C, F) catalysts; GHSV = 60,000 h⁻¹; catalyst amount: 100 mg.

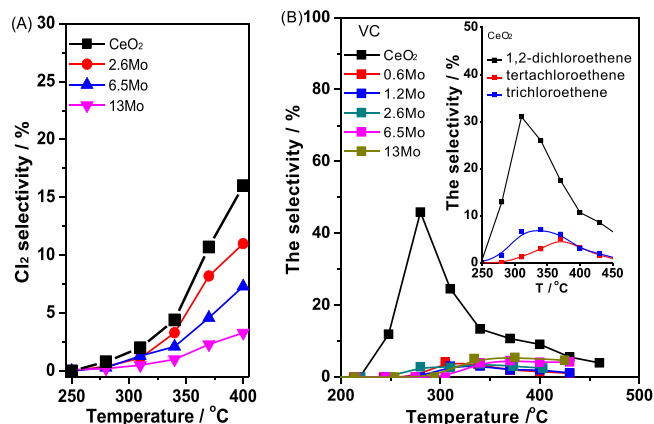


Fig. 9. The product distributions during 1,2-DCE oxidation: the selectivity for Cl₂ (A) and chlorinated compounds (B); gas composition: 1000 ppm 1,2-DCE, 10% O₂ and N₂ balance; GHSV = 60,000 h⁻¹; catalyst amount: 100 mg.

over 6.5Mo and 13Mo catalysts increases slightly to 5% at 300 °C, due probably to their poor activity for VC oxidation. In the stability test at 250 °C, Mo₆O₁₃/CeO₂ catalysts maintain a stable selectivity for VC below 5%, of which only 0.6Mo and 1.2Mo catalysts with significantly exposed CeO₂ present 1% or less selectivity for polychloroethylene, which is much lower than CeO₂. When the conversion approaches 90%, polychloroethylene is not detected over 0.6Mo and 1.2Mo catalysts within FID limitation (1 ppm). No any chlorination products over the catalysts with 2.6Mo atom/nm² or higher can be detected. The inhibited chlorination suggests that 1,2-DCE adsorption and activation occur mainly on the sites related to (O=)₂Mo-(O-Ce)₂ species, where Cl removal is quick. Cl deposition should occur on the exposed CeO₂. As reported, Mo-Cl

strength is 72 kcal/mol, while Mo-O, 145 kcal/mol [46,47]. On the other hand, the dissociation of water produced during the reaction increases the availability of hydroxyl groups and protons on MoO_x/CeO₂. These features of (O=)₂Mo-(O-Ce)₂ species are favorable for Cl removal. The CO₂ selectivity is in a range of 70 – 80%. CeO₂ presents CO₂ selectivity of 80% or higher. As recently reported (Table S4) for 1,2-DCE catalytic combustion, high selectivity for CO_x (no chlorination) was obtained on some Cr-based and Ru-based catalysts. However, MoO_x/CeO₂ catalysts with (O=)₂Mo-(O-Ce)₂ present the excellent performance in a broader range of reactant concentrations at higher GHSV, including high activity, stability and high selectivity for CO/CO₂ (no chlorination), which will be desirable for industrial application.

3.5. The activity of 2.6Mo catalysts and Pt's action in wet feed

In wet feed containing 5% V/V water, 1,2-DCE conversion to CO_x below 200 °C over CeO₂ increases slightly (Fig. 10A), which is assigned to the promoted Cl removal [48]. However, the negative effect of water is observed at 200 °C or higher with T₅₀ increasing from 380 to 415 °C, and the conversion cannot approach compete within the experimental temperature. OH⁻ formed during water dissociation competes with oxygen for adsorption sites as if Cl species does over CeO₂ in dry feed, which makes the formation of surface oxygen and Cl deposition rather difficult. Lykhach et al. found the existing of hydroxyl groups on CeO₂ at 700 K in SRPES spectra [49]. Here, the formed basic Ce-OH, the decrease in ability for oxidation and chlorination of VC are all favorable for the formation of VC (Fig. S19A). For 2.6Mo catalyst, the negative effect of water is small, and T₉₀ increases only to 320 °C from 281 °C in dry feed (Fig. 10B). In fact, the (O=)₂Mo-(O-Ce)₂ species is transformed into [MoO₄]²⁻ or [Mo₇O₂₄]⁶⁻ anions in wet feed (Fig. 1, Fig. S3), where strong Lewis acid can become weak. However, the promoted water dissociation increases Mo-OH group with Brønsted acid [19], which

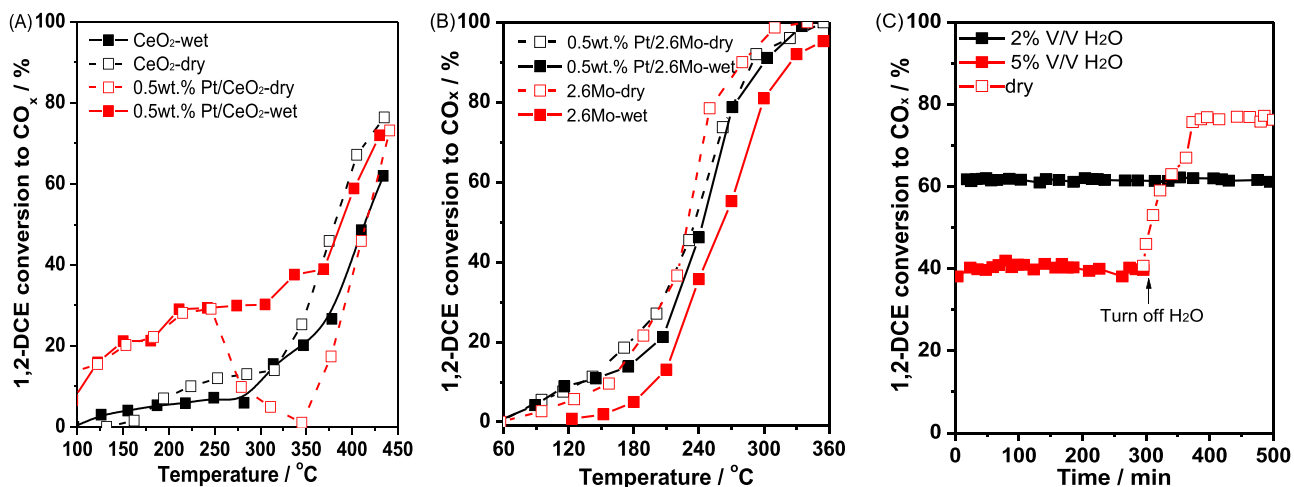


Fig. 10. The 1,2-DCE conversion curves in dry and wet feed (5%V/V H₂O) over CeO₂ and 0.5 wt%Pt/CeO₂ catalysts (A), 2.6Mo and 0.5 wt%Pt/2.6Mo catalysts (B) and the stability of 2.6Mo catalyst on the stream feed containing 2% and 5% V/V H₂O (C); gas composition: 1000 ppm 1,2-DCE, 10% O₂ and N₂ balance; GHSV = 60,000 h⁻¹; catalyst amount: 100 mg.

promote the hydration of 1,2-DCE into -O-CH₂-CH₂-O- or further into carboxylates. Chlorinated alkane could be hydrated into alkoxy group on hydroxyl groups [17,18]. The selectivity for VC increases at low temperature to some extent (Fig. S19), indicating that the formation of VC is related to weak acid. In order to investigate the action of surface oxygen in the reaction in wet feed, CeO₂ and 2.6Mo catalyst were loaded by 0.5 wt% Pt (high resistant to water) to promote the adsorption and activation of gas oxygen under humid condition [50]. It is interesting to find that the activity of 0.5 wt%Pt/2.6Mo in wet feed can be maintained at the level in dry feed of 2.6Mo (Fig. 10B), indicating that the availability of surface oxygen is critical to 1,2-DCE wet oxidation over MoO_x/CeO₂ catalysts. Moreover, Pt addition cannot change the product distribution, especially for chlorination products. It should be noted that 1,2-DCE conversion to CO_x over 0.5 wt%Pt/CeO₂ in dry feed is low, which can be ascribed to high activity of Pt-O-Ce species for chlorination [21]. 0.5 wt%Pt/CeO₂ presents the promoted activity only in wet feed, especially at low temperature, where the chlorination decreases (Fig. S20). No any chlorination is observed over 0.5 wt%Pt/2.6Mo in wet or dry feed, which further verified that Cl deposition is considered to be ignored so that the chlorination with Pt presence cannot occur (Fig. S20). During the stability test in wet feed, 2.6Mo catalyst presents stable wet activity, although the conversion at 250 °C decreases from 80% in dry feed to 60% at 2%V/V water (500 min) and 40% at 5% V/V water (300 min) (Fig. 10C). 2.6Mo catalyst in 5% V/V water feed can restore within 100 min after turning off water, indicating that [MoO₄]²⁻ or [Mo₇O₂₄]⁶⁻ anions on CeO₂ in wet feed is highly stable and the transformation between (O=)₂Mo(O-Ce)₂ in dry and [MoO₄]²⁻ or [Mo₇O₂₄]⁶⁻ anions in wet feed is reversible.

4. Conclusion

MoO_x/CeO₂ catalysts with Mo loading of 0.9–12.0 wt% prepared by wetness were investigated in terms of their relation of structure with catalytic performance for 1,2-DCE oxidation. Characterization reveals that Mo species loaded on fluorite CeO₂ exists as (O=)₂Mo(O-Ce)₂, poly dioxo MoO₄ and MoO₃ particles. The Mo-O-Ce formed through MoO_x-CeO₂ interaction increases O₂²⁻ species, promotes the reducibility of Mo species and Lewis acidity, while O₂⁻ and O[·] surface oxygen species are mainly contribution from CeO₂. In situ FT-IR shows that 1,2-DCE adsorbs on the sites related to (O=)₂Mo-(O-Ce)₂ through the formation of acetyl species, which is oxidized into carboxylates with the acetate type, and then into carbonate by surface oxygen. The promoted water dissociation with O₂ presence is observed over the catalysts with (O=)₂Mo(O-Ce)₂. MoO_x/CeO₂ catalysts exhibit high stable activity for 1,2-DCE

oxidation with TOF_{Mo} at 250 °C is $0.7 - 3.2 \times 10^{-3} \text{ s}^{-1}$ and T₉₀ below 320 °C at 1000–2000 ppm 1,2-DCE and 2.5–20% O₂ at 60,000 space velocity. High resistance to Cl species keeps high accessibilities of both surface oxygen and acidity, whose synergism is critical for 1,2-DCE activation and oxidation. Main products over MoO_x/CeO₂ are composed of CO_x, HCl, H₂O and trace VC, and the chlorination is almost completely inhibited. Strong Cl adsorption on CeO₂ catalyst results in low activity for 1,2-DCB oxidation and low selectivity for CO_x.

CRediT authorship contribution statement

Xingyi Wang: conceived and designed this study. **Yanglong Guo:** drafted manuscript and designed equipment. **Hao Zhang:** performed experiments and collected data. **Xiaohui Gao:** treated data and performed Py-FT-IR tests. **Binwei Gong:** performed activity experiments. **Shijie Shao:** data treatment. **Chensheng Tu:** performed some stability tests. **Jun Pan and Yangyang Wang:** computer software. **Qiguang Dai:** reviewed manuscript and checked English.

Declaration of Competing Interest

The authors declare that they have no known competing financial interests or personal relationships that could have appeared to influence the work reported in this paper.

Acknowledgments

We would like to acknowledge the National Natural Science Foundation of China (no. 21976056, 21777043 and 21922602).

Appendix A. Supporting information

Supplementary data associated with this article can be found in the online version at [doi:10.1016/j.apcatb.2022.121240](https://doi.org/10.1016/j.apcatb.2022.121240).

References

- [1] F.W. Lin, Z.M. Zhang, N. Li, B.B. Yan, C. He, Z.P. Hao, G.Y. Chen, How to achieve complete elimination of Cl-VOCS: a critical review on byproducts formation and inhibition strategies during catalytic oxidation, *Chem. Eng. J.* 404 (2021), 126534, <https://doi.org/10.1016/j.cej.2020.126534>.
- [2] H. Liu, X. Li, Q.G. Dai, H.L. Zhao, G.T. Chai, Y.L. Guo, Y. Guo, L. Wang, W.C. Zhan, Catalytic oxidation of chlorinated volatile organic compounds over Mn-Ti composite oxides catalysts: elucidating the influence of surface acidity, *Appl. Catal. B: Environ.* 282 (2021), 119577, <https://doi.org/10.1016/j.apcatb.2020.119577>.

[3] J.M. Giraudon, A. Elhachimi, G. Leclercq, Catalytic oxidation of chlorobenzene over Pd/perovskites, *Appl. Catal. B: Environ.* 84 (2008) 251–261, <https://doi.org/10.1016/j.apcatb.2008.04.023>.

[4] A. Aranzabal, J.A. González-Marcos, M. Romero-Sáez, J.R. González-Velasco, M. Guillermot, P. Magnoux, Stability of protonic zeolites in the catalytic oxidation of chlorinated VOCs (1,2-dichloroethane), *Appl. Catal. B: Environ.* 88 (2009) 533–541, <https://doi.org/10.1016/j.apcatb.2008.10.007>.

[5] T. Cai, H. Huang, W. Deng, Q.G. Dai, W. Liu, X.Y. Wang, Catalytic combustion of 1,2-dichlorobenzene at low temperature over Mn-modified Co_3O_4 catalysts, *Appl. Catal. B: Environ.* 166–167 (2015) 393–405, <https://doi.org/10.1016/j.apcatb.2014.10.047>.

[6] L. Li, J.W. Shi, M.J. Tian, C.W. Chen, B.R. Wang, M.D. Ma, C. He, In situ fabrication of robust three dimensional ordered macroporous $\gamma\text{-Mn}_2/\text{LaMnO}_{3.15}$ catalyst for chlorobenzene efficient destruction, *Appl. Catal. B: Environ.* 282 (2021) 119565, <https://doi.org/10.1016/j.apcatb.2020.119565>.

[7] Y.M. Jiao, X. Chen, F. He, S.T. Liu, Simple preparation of uniformly distributed mesoporous Cr/TiO₂ microspheres for low-temperature catalytic combustion of chlorobenzene, *Chem. Eng. J.* 372 (2019) 107–117, <https://doi.org/10.1016/j.cej.2019.04.118>.

[8] Z. Zhang, J. Huang, H.Q. Xia, Q.G. Dai, Y.F. Gu, Y.J. Lao, X.Y. Wang, Chlorinated volatile organic compound oxidation over $\text{SO}_4^{2-}/\text{Fe}_2\text{O}_3$ catalysts, *J. Catal.* 360 (2018) 277–289, <https://doi.org/10.1016/j.jcat.2017.11.024>.

[9] H. Huang, Y.F. Gu, J. Zhao, X.Y. Wang, Catalytic combustion of chlorobenzene over VO_x/CeO_2 catalysts, *J. Catal.* 326 (2015) 54–68, <https://doi.org/10.1016/j.jcat.2015.02.016>.

[10] X.Y. Wang, Q. Kang, D. Li, Catalytic combustion of chlorobenzene over $\text{MnO}_x/\text{CeO}_2$ mixed oxide catalysts, *Appl. Catal. B: Environ.* 86 (2009) 166–175, <https://doi.org/10.1016/j.apcatb.2008.08.009>.

[11] A.P. Amrute, C. Mondelli, M. Moser, G. Novell-Leruth, N. López, D. Rosenthal, R. Farra, M.E. Schuster, D. Teschner, T. Schmidt, J. Pérez-Ramírez, Performance, structure, and mechanism of CeO_2 in HCl oxidation to Cl_2 , *J. Catal.* 286 (2012) 287–297, <https://doi.org/10.1016/j.jcat.2011.11.016>.

[12] H. Huang, Q.G. Dai, X.Y. Wang, Morphology effect of Ru/CeO₂ catalysts for the catalytic combustion of chlorobenzene, *Appl. Catal. B: Environ.* 158–159 (2014) 96–105, <https://doi.org/10.1016/j.apcatb.2014.01.062>.

[13] Z. Zhao, X.T. Gao, I.E. Wachs, Comparative study of bulk and supported V–Mo–Te–Nb–O mixed metal oxide catalysts for oxidative dehydrogenation of propane to propylene, *J. Phys. Chem. B* 107 (2003) 6333–6342, <https://doi.org/10.1021/jp021640m>.

[14] D.L. Stern, R.K. Grasselli, Propane oxydehydrogenation over molybdate-based catalysts, *J. Catal.* 167 (1997) 550–559, <https://doi.org/10.1006/jcat.1997.1568>.

[15] W.E. Farneth, R.H. Staley, P.J. Domaille, R.D. Farlee, Comparison of structure and thermal chemistry of stoichiometric and catalytic alkoxy-substituted molybdenum heteropolyanions: carbon-13 CP-MAS NMR spectrum of a chemisorbed reaction intermediate, *J. Am. Chem. Soc.* 109 (1987) 4018–4023, <https://doi.org/10.1021/ja00247a030>.

[16] X.L. Tang, Y.R. Shi, F.Y. Gao, S.Z. Zhao, H.H. Yi, Z.L. Xie, Promotional role of Mo on $\text{Ce}_{0.3}\text{FeO}_x$ catalyst towards enhanced $\text{NH}_3\text{-SCR}$ catalytic performance and SO_2 resistance, *Chem. Eng. J.* 398 (2020), 125619, <https://doi.org/10.1016/j.cej.2020.125619>.

[17] J. Zhao, W.J. Xi, C.S. Tu, Q.G. Dai, X.Y. Wang, Catalytic oxidation of chlorinated VOCs over Ru/Ti_xSn_{1-x} catalysts, *Appl. Catal. B: Environ.* 263 (2020), 118237, <https://doi.org/10.1016/j.apcatb.2019.118237>.

[18] W. Sun, B.W. Gong, J. Pan, Y.Y. Wang, H.Q. Xia, H. Zhang, Q.G. Dai, L. Wang, X. Y. Wang, Catalytic combustion of CVOCs over $\text{Cr}_x\text{Ti}_{1-x}$ oxide catalysts, *J. Catal.* 391 (2020) 132–144, <https://doi.org/10.1016/j.jcat.2020.08.007>.

[19] F. Di-Grégorio, V. Keller, T. Di-Costanzo, J.L. Vignes, D. Michel, G. Maire, Cracking and skeletal isomerization of hexenes on acidic $\text{MoO}_3\text{-WO}_3/\alpha\text{-Al}_2\text{O}_3$ oxide, *Appl. Catal. A: Gen.* 218 (2001) 13–24, [https://doi.org/10.1016/S0926-860X\(01\)00587-7](https://doi.org/10.1016/S0926-860X(01)00587-7).

[20] X. Liu, W.Y. Zhang, M.G. Peng, G.Q. Zhai, L.C. Hu, L.Q. Mao, The role of S and Mo doping on the dissociation of water molecule on FeOCl surface: experimental and theoretical analysis, *Chem. Eng. J.* 426 (2021), 131353, <https://doi.org/10.1016/j.cej.2021.131353>.

[21] Y.F. Gu, T. Cai, X.H. Gao, H.Q. Xia, W. Sun, J. Zhao, Q.G. Dai, X.Y. Wang, Catalytic combustion of chlorinated aromatics over WO_x/CeO_2 catalysts at low temperature, *Appl. Catal. B: Environ.* 248 (2019) 264–276, <https://doi.org/10.1016/j.apcatb.2018.12.055>.

[22] J.R. González-Velasco, R. López-Fonseca, A. Aranzabal, J.I. Gutiérrez-Ortiz, P. Steltenpohl, Evaluation of H-type zeolites in the destructive oxidation of chlorinated volatile organic compounds, *Appl. Catal. B: Environ.* 24 (2000) 233–242, [https://doi.org/10.1016/S0926-3373\(99\)00105-8](https://doi.org/10.1016/S0926-3373(99)00105-8).

[23] E. Cheng, J. Notestein, Catalytic dehydrogenation of isobutane over supported $\text{MoO}_x/\text{K-Al}_2\text{O}_3$, *J. Catal.* 397 (2021) 212–222, <https://doi.org/10.1016/j.jcat.2021.03.032>.

[24] M. Daniel, S. Loridant, Probing reoxidation sites by in situ Raman spectroscopy: differences between reduced CeO_2 and Pt/CeO_2 , *J. Raman Spectrosc.* 43 (2012) 1312–1319, <https://doi.org/10.1002/jrs.4030>.

[25] W. Deng, Q. Dai, Y. Lao, B. Shi, X. Wang, Low temperature catalytic combustion of 1,2-dichlorobenzene over $\text{CeO}_2\text{-TiO}_2$ mixed oxide catalysts, *Appl. Catal. B: Environ.* 181 (2016) 848–861, <https://doi.org/10.1016/j.apcatb.2015.07.053>.

[26] G. Dutta, U.V. Waghmare, T. Baidya, M.S. Hegde, K.R. Priolkar, P.R. Sarode, Origin of enhanced reducibility/oxygen storage capacity of $\text{Ce}_{1-x}\text{Ti}_x\text{O}_2$ compared to CeO_2 or TiO_2 , *Chem. Mater.* 18 (2006) 3249–3256, <https://doi.org/10.1021/cm060267i>.

[27] E.L. Lee, I.E. Wachs, In situ spectroscopic investigation of the molecular and electronic structures of SiO_2 supported surface metal oxides, *J. Phys. Chem. C* 111 (2007) 14410–14425, <https://doi.org/10.1021/jp0735482>.

[28] X.Z. Du, L. Dong, C. Li, Y.Q. Liang, Y. Chen, Diffuse reflectance infrared Fourier transform and Raman spectroscopic studies of MoO_3 dispersed on CeO_2 support, *Langmuir* 15 (1999) 1693–1697, <https://doi.org/10.1021/la980697q>.

[29] H.J. Tian, C.A. Roberts, I.E. Wachs, Molecular structural determination of molybdena in different environments: aqueous solutions, bulk mixed oxides, and supported MoO_3 catalysts, *J. Phys. Chem. C* 114 (2010) 14110–14120, <https://doi.org/10.1021/jp103269w>.

[30] W.P. Griffith, P.J.B. Lesniak, Raman studies on species in aqueous solutions. Part III. Vanadates, molybdates, and tungstates, *J. Chem. Soc. A* (1969) 1066–1071, <https://doi.org/10.1039/J19690001066>.

[31] H. Hu, I.E. Wachs, S.R. Bare, Surface structures of supported molybdenum oxide catalysts: characterization by Raman and Mo L₃-edge XANES, *J. Phys. Chem. C* 99 (1995) 10897–10910, <https://doi.org/10.1021/j100027a034>.

[32] I. Julian, M. Roedern, J. Hueso, S. Irusta, A. Baden, R. Mallada, Z. Davis, J. Santamaría, Supercritical solvothermal synthesis under reducing conditions to increase stability and durability of Mo/ZSM-5 catalysts in methane dehydroaromatization, *Appl. Catal. B: Environ.* 263 (2020), 118360, <https://doi.org/10.1016/j.apcatb.2019.118360>.

[33] Y. Nagai, K. Dohmae, Y.F. Nishimura, H. Kato, H. Hirata, N. Takahashi, Operando XAFS study of catalytic NO reduction over Cu/CeO_2 : the effect of copper–ceria interaction under periodic operation, *Phys. Chem. Chem. Phys.* 15 (2013) 8461–8465, <https://doi.org/10.1039/C3CP44316G>.

[34] M. Daniel, S. Loridant, Probing reoxidation sites by in situ Raman spectroscopy: differences between reduced CeO_2 and Pt/CeO_2 , *Raman Spectrosc.* 43 (2012) 1312–1319, <https://doi.org/10.1002/jrs.4030>.

[35] Z. Wu, M. Li, J. Howe, H. Overbury, Probing defect sites on CeO_2 nanocrystals with well-defined surface planes by Raman spectroscopy and O_2 adsorption, *Langmuir* 26 (2010) 16595–16606, <https://doi.org/10.1021/la101723w>.

[36] M. Iwasaki, E. Iglesia, Mechanistic assessments of NO oxidation turnover rates and active site densities on WO_3 -promoted CeO_2 catalysts, *J. Catal.* 342 (2016) 84–97, <https://doi.org/10.1016/j.jcat.2016.07.011>.

[37] A. Chakrabarti, I.E. Wachs, Molecular structure–reactivity relationships for olefin metathesis by Al_2O_3 -supported surface MoO_x sites, *ACS Catal.* 8 (2018) 949–959, <https://doi.org/10.1021/acscatal.7b03598>.

[38] S. Enomoto, M. Asahina, Infrared spectra of vinyl chloride and its deuterated derivatives, *J. Mol. Spectrosc.* 19 (1966) 117–130, [https://doi.org/10.1016/0022-2852\(66\)90235-9](https://doi.org/10.1016/0022-2852(66)90235-9).

[39] M. Rodler, C.E. Blom, A. Bauder, Infrared spectrum and general valence force field of syn-vinyl alcohol, *J. Am. Chem. Soc.* 106 (1984) 4029–4035, <https://doi.org/10.1021/ja00326a025>.

[40] D. Demri, J.-P. Hindermann, C. Diagne, A. Kiennemann, Formation of C_2 oxygenates on rhodium-containing catalysts during $\text{CO} + \text{H}_2$ reactions. FTIR study of acetaldehyde adsorption, *J. Chem. Soc., Faraday Trans.* 90 (1994) 501–506, <https://doi.org/10.1039/FT9949000501>.

[41] V. Sanchez Escribano, G. Busca, V. Lorenzelli, Fourier transform infrared spectroscopic studies of the reactivity of vanadia-titania catalysts toward olefins. 1. Propylene, *J. Phys. Chem. C* 94 (1990) 8939–8945, <https://doi.org/10.1021/j100389a017>.

[42] Y. Maréchal, IR spectra of carboxylic acids in the gas phase: a quantitative reinvestigation, *J. Chem. Phys.* 87 (1987) 6344–6353, <https://doi.org/10.1063/1.453464>.

[43] J.M. Stencel, L.E. Makovsky, T.A. Sarkus, J. de Vries, R. Thomas, J.A. Moulijn, Raman spectroscopic investigation of the effect of H_2O on the molybdenum surface species in $\text{MoO}_3\text{Al}_2\text{O}_3$ catalysts, *J. Catal.* 90 (1984) 314–322, [https://doi.org/10.1016/0021-9517\(84\)90259-8](https://doi.org/10.1016/0021-9517(84)90259-8).

[44] S.J. Feng, J. Zhao, Y.J. Bai, X.X. Liang, T. Wang, C.Y. Wang, Facile synthesis of Mo-doped TiO_2 for selective photocatalytic CO_2 reduction to methane: Promoted H_2O dissociation by Mo doping, *J. CO₂ Util.* 38 (2020) 1–9, <https://doi.org/10.1016/j.jcou.2019.12.019>.

[45] Q.G. Dai, L.L. Yin, S.X. Bai, W. Wang, X.Y. Wang, X.Q. Gong, G.Z. Lu, Catalytic total oxidation of 1,2-dichloroethane over VO_x/CeO_2 catalysts: further insights via isotopic tracer techniques, *Appl. Catal. B: Environ.* 182 (2016) 598–610, <https://doi.org/10.1016/j.apcatb.2015.10.016>.

[46] S.P. Nolan, R.L. De La Vega, C.D. Hoff, Heats of reaction of $\text{HMo}(\text{CO})_3\text{C}_5\text{H}_5$ with CCl_4 and CBr_4 and of $\text{NaMo}(\text{CO})_3\text{C}_5\text{H}_5$ with I_2 and CH_3 . solution thermochemical study of the Mo–X bond for X = H, Cl, Br, I and CH_3 , *J. Organomet. Chem.* 315 (1986) 187–199, [https://doi.org/10.1016/0022-328X\(86\)80437-5](https://doi.org/10.1016/0022-328X(86)80437-5).

[47] J. Speight, *Lange's Handbook of Chemistry*, seventeenth ed., McGraw Hill Education, New York, 2017.

[48] C.E. Hetrick, F. Patcas, M.D. Amiridis, Effect of water on the oxidation of dichlorobenzene over $\text{V}_2\text{O}_5/\text{TiO}_2$ catalysts, *Appl. Catal. B: Environ.* 101 (2011) 622–628, <https://doi.org/10.1016/j.apcatb.2010.11.003>.

[49] Y. Lykhach, V. Johánek, H.A. Aleksandrov, S.M. Kozlov, M. Happel, T. Skála, P. S. Petkov, N. Tsud, G.N. Vayssilov, K.C. Prince, K.M. Neyman, V. Matolín, J. Libuda, Water chemistry on model ceria and Pt/ceria catalysts, *J. Phys. Chem. C* 116 (2012) 12103–12113, <https://doi.org/10.1021/jp302229x>.

[50] L. Gutierrez, A. Boix, J. Petunchi, Effect of Pt on the water resistance of Co-zeolites upon the SCR of NO_x with CH_4 , *Catal. Today* 54 (1999) 451–464, [https://doi.org/10.1016/s0920-5861\(99\)00208-4](https://doi.org/10.1016/s0920-5861(99)00208-4).